

# Numerical study of transverse position monitor and compensation for x-ray polarization diagnosis

Zipeng Liu,<sup>1,2</sup> Bangjie Deng,<sup>3</sup> Haixiao Deng,<sup>4,\*</sup> and Bo Liu<sup>4</sup>

<sup>1</sup>Shanghai Institute of Applied Physics, Chinese Academy of Sciences, China

<sup>2</sup>University of Chinese Academy of Sciences, China

<sup>3</sup>Xi'an Jiaotong University, School of Nuclear Science and Technology, China

<sup>4</sup>Shanghai Advanced Research Institute, Chinese Academy of Sciences, China

(Dated: April 21, 2021)

Diagnosing free electron laser (FEL) polarization is critical for polarization-modulated research such as x-ray free electron laser (XFEL) diffraction imaging and probing material magnetism. In an electron time-of-flight (eTOF) polarimeter, the flight time and angular distribution of photoelectrons were designed based on x-ray polarimetry for on-site diagnosis. However, the transverse position of x-ray FEL pulses introduces error into the measured photoelectron angular distribution. This work thus proposes a method to monitor the transverse position using an eTOF polarimeter and explains how to compensate for the error due to transverse position. A comprehensive numerical model is developed to demonstrate the feasibility of the compensation method, and the results reveal that a spatial resolution of 20  $\mu\text{m}$  and a polarity improved by 0.5% is possible with fully polarized FEL pulses. The impact of FEL pulses and a method to calibrate their linearity is also discussed.

## I. INTRODUCTION

Being fully coherent and offering controlled polarization [1–4], the x-ray free electron laser (XFEL) is at the heart of advanced techniques in fields such as materials science and surface physics. Currently, several XFELs machines have been constructed or are in operation [5–8]. The diagnosis of XFEL pulse polarization is critical in research involving polarization-modulated diffraction and spectroscopy [9–12]. Several methods are available to measure the x-ray polarization of XFEL pulses, including phase-shift retarders [13–17] and angular-distribution-based polarimeters [3, 18]. In particular, the time of flight and angular distribution of photoelectrons produced by x-ray polarimeters are used for on-site diagnosis, in so-called 'eTOF polarimeters'. Such instruments have been used in main FEL facilities [19–21]. The Shanghai soft-x-ray FEL facility [22] is currently offline testing an eTOF-like prototype for angular-resolved polarimeter (ARPolar). However, variations in the incident position of XFEL pulse may distort the photoelectron's angular distribution and thus invalidate the resulting polarization diagnosis.

A single-shot x-ray beam-position monitor (XBPM) is essential for XFEL diagnosis and experimentation. Various XBPMs have been developed in FEL facilities, such as fluorescence detectors [23, 24], ion chambers [25], and backscattering photodiodes [26]. However, the low intensity of the soft XFEL makes it difficult to use the fluorescence screen and backscattering methods to determine beam position. Although another ion chamber nearer the eTOF polarimeter may be used to obtain the transverse position, it is hard to rearrange the machine. Therefore, the shot-to-shot transverse position must be measured so that the error term may be compensated.

Since monitoring transverse position and polarity are both indispensable for XFEL experiments, the ARPolar device must offer these two functions. This work thus proposes an

on-site single-shot x-ray beam position monitoring and polarization compensation method using the ARPolar polarimeter. The methods and principles are first described, following which a comprehensive numerical model is established to validate the method, and the calibration method is presented. Finally, the key factors are discussed, including detector linearity and photoelectron yield.

## II. PRINCIPLES AND METHODS

Figure 1 shows the ARPolar instrument, which consists of a chamber, 16 detection channels, two gas-injection assemblies, and two turbo pumps. Each channel contains three groups of electrodes, a magnetism-shielded flight tube, and a microchannel plate detector (MCP). Electrons produced by XFEL pulses ionize a gas target in the center of the chamber. The electrons are dipole-symmetrical in the plane perpendicular to the beam-line (detection plane), from which the polarization characteristics of the XFEL pulses can be obtained. The angular distribution can be divided into four identical ranges, starting from the polarization angle and then incrementing by  $\pi/2$ . However, this symmetry in the angular distribution changes when the x-ray pulses are displaced from the center of the beamline pipe. By solving for the incident positions, both the real detection direction and the correct charge distribution can be predicted. Furthermore, the linear polarity can be compensated accordingly. The corresponding principles and the methods are presented here.

Considering the incident position  $P(r, \theta)$ , the charge  $Q(r, \theta)$  detected in the detection plane can be written as

$$Q(r, \theta) = \int \frac{p(\gamma)}{\rho^2} d\gamma, \quad (1)$$

$$\gamma(r, \theta) = \arccos \left( \frac{R \cos \gamma - \gamma \cos \theta}{\sqrt{R^2 + r^2 - Rr \sin(\theta - \gamma)}} \right), \quad (2)$$

where  $p(\gamma)$  is the angular distribution of electrons,  $\rho$  is the distance from the pulse center to the detection hole of the chan-

\* denghaixiao@zjlab.org.cn

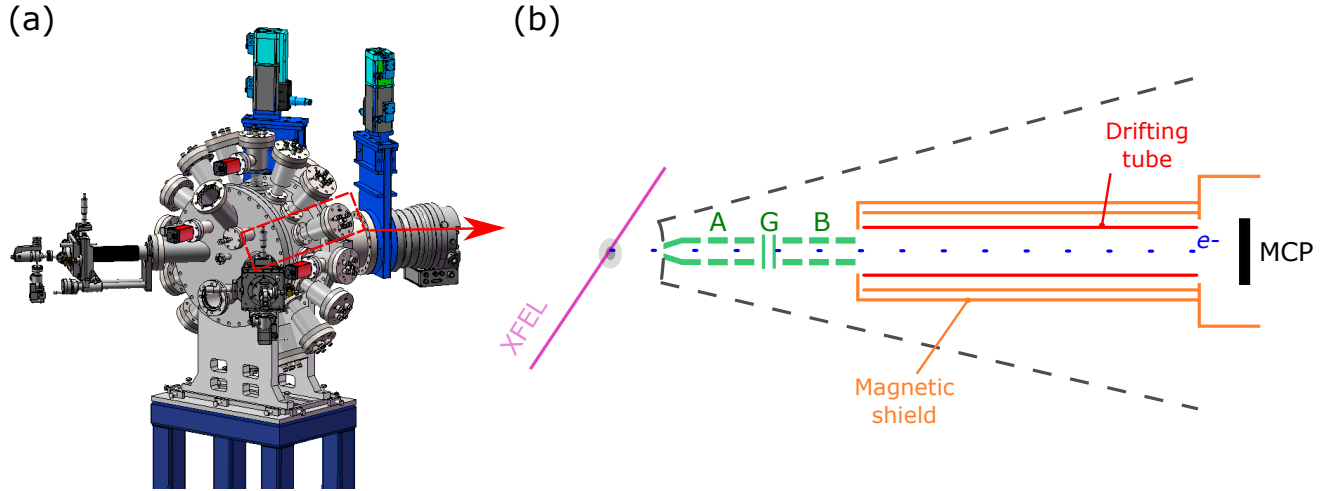


FIG. 1. The ARPolar instrument: (a) drawing of instrument, (b) scheme of a detection channel, positioned in red square in panel (a). Detection channel consists of focusing electrode groups (A and B), retarding grid electrodes (G), magnetic shields, a drift tube, and a MCP detector.

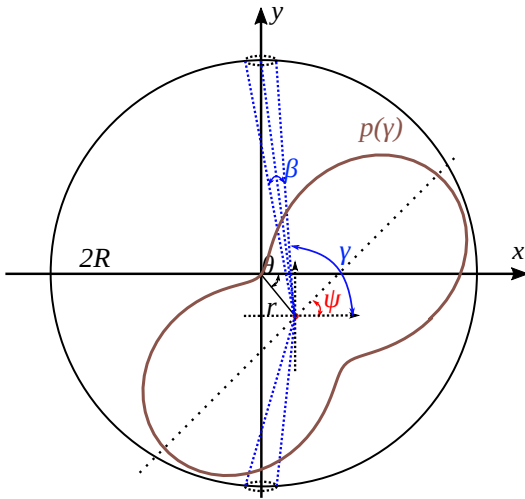


FIG. 2. Diagram of detection angle.

nel,  $r$  is the relative displacement between the device center and the x-ray pulse,  $R$  is the distance from the front tube to the device center,  $\theta$  is the angular direction of the incident position, and  $\gamma$  is the angular direction of the detector (see Fig. 2). The horizontal and vertical axes divide the electrons into four quadrants,

$$Q_i = \int_{\psi+\pi(i-1)/2}^{\psi+\pi i/2} \frac{p(\gamma)}{\rho^2} d\gamma, \quad i = 1, \dots, 4, \quad (3)$$

where  $\psi$  is the polarization angle of the x-ray pulse, which is determined by the undulator configuration. When  $\psi = 0$ , the position sensitivities  $S_x$  and  $S_y$ , which are the proportionality constants between charge and pulse displacement, are defined

as [27, 28]

$$S_x = \frac{d}{dx} \left( \frac{\Delta Q_{x, \psi=0}}{\sum Q} \right) = \frac{d\eta_{x, \psi=0}}{dx}, \quad (4)$$

$$S_y = \frac{d}{dy} \left( \frac{\Delta Q_{y, \psi=0}}{\sum Q} \right) = \frac{d\eta_{y, \psi=0}}{dy}, \quad (5)$$

where  $S_x$  and  $S_y$  refer to the horizontal and vertical directions, respectively. Furthermore,

$$\Delta Q_x = (Q_1 + Q_4) - (Q_2 + Q_3), \quad (6)$$

$$\Delta Q_y = (Q_1 + Q_2) - (Q_3 + Q_4), \quad (7)$$

$$\sum Q_x = Q_1 + Q_2 + Q_3 + Q_4, \quad (8)$$

$$\eta_x = \frac{\Delta Q_x}{\sum Q}, \quad (9)$$

$$\eta_y = \frac{\Delta Q_y}{\sum Q}. \quad (10)$$

The relation  $x(\eta_x)$  can be expanded as a Taylor series about  $\eta_x = 0$ :

$$x(\eta_x) = x(\eta_x = 0) + x'(\eta_x)\eta_x + O(\eta_x), \quad (11)$$

where  $\eta_x = 0$  indicates  $\Delta Q_x = 0$  and  $\hat{x} = 0$ . Thus, the incident position  $(\hat{x}, \hat{y})$

$$\hat{x} \approx \frac{1}{S_x} \eta_x + \delta_x, \quad (12)$$

$$\hat{y} \approx \frac{1}{S_y} \eta_y + \delta_y. \quad (13)$$

where  $\delta_x$  and  $\delta_y$  refer to the contribution of  $O(\eta_x)$  and  $O(\eta_y)$ , respectively. In  $x$ - $y$  coordinates, the real position  $(x, y)$  is obtained by rotating an angle  $\psi$ , as follows:

$$\begin{bmatrix} x \\ y \end{bmatrix} = \begin{bmatrix} \cos(\psi) & -\sin(\psi) \\ \sin(\psi) & \cos(\psi) \end{bmatrix} \begin{bmatrix} \hat{x} \\ \hat{y} \end{bmatrix}. \quad (14)$$

In the vertical plane through the beamline, the angular distribution  $p_s(\gamma)$  of  $s$ -shell photoelectrons can be described in the dipole approximation as [19, 29, 30]

$$p_s(\gamma) = A\{1 + P_l \cos[2(\gamma - \psi)]\}, \quad (15)$$

where  $A$  is the normalization constant;  $P_l$  and  $\psi$  are the linear polarity and the polarization angle of the FEL, respectively. The polarization characteristics of the XFEL can be obtained by fitting the angular charge distribution monitored by detectors to Eq. (15). For the incident position  $(\hat{x}_i, \hat{y}_i)$ . The average probability density  $\bar{p}(\gamma_i)$  is

$$\bar{p}_s(\gamma_i) = \frac{Q_{s,i}}{\beta_i} = \int_{\gamma_{i,-}}^{\gamma_{i,+}} p_s(\gamma) d\gamma, \quad (16)$$

where  $Q_{s,i}$  is the number of charges collected by detector  $i$ ,  $\beta_i$  is the collection angle of detector  $i$ , and  $\bar{p}(\gamma_i)$  is the average probability density for  $\beta_i$  and is formed using Eq. (15). The charges detected by detector  $i$  can then be found by using Eq. (16). Fitting the data to Eq. (15) gives the new linear polarity and polarization angle.

### III. NUMERICAL MODEL

To validate the method described above, we developed a comprehensive numerical model. A Monte Carlo model was developed to simulate the yield and angular distribution of photoelectrons, whose primary photon source was configured according to a start-to-end simulation of the FEL in self-amplified spontaneous emission (SASE) mode. The vertices of the photoelectrons and Auger electrons were recorded to simulate electron transmission, which was coupled with the static electric field to obtain the flight trajectories and collection efficiency of the electron-optical system of the ARPolar soft-x-ray-FEL (SXFEL) polarimeter. In the following, the model is described in detail.

#### A. Model setup

The full process of the SASE-mode FEL was simulated to produce FEL pulses based on the configuration of the SASE line of the Shanghai SXFEL, has an electron-beam energy of 1.6 GeV and an undulator period  $\lambda_u = 16$  mm. The center wavelength  $\lambda_s$  of the XFEL pulse can be determined from the resonance condition:

$$\lambda_s = \frac{\lambda_u}{2\gamma^2} \left(1 + \frac{K^2}{2}\right), \quad (17)$$

where  $\gamma$  is the electron-beam Lorentz factor and  $K$  is the field parameter of the undulator. This process was simulated by the well-benchmarked FEL code GENESIS. The root-mean-square (RMS) value of the transverse diameter of the pulse is 200  $\mu\text{m}$  and the energy spectrum of the FEL pulse is shown in Fig. 3. The simulation indicates the saturation power is on the order of  $10^9$  W and that each FEL pulse contains  $1.133 \times 10^{12}$

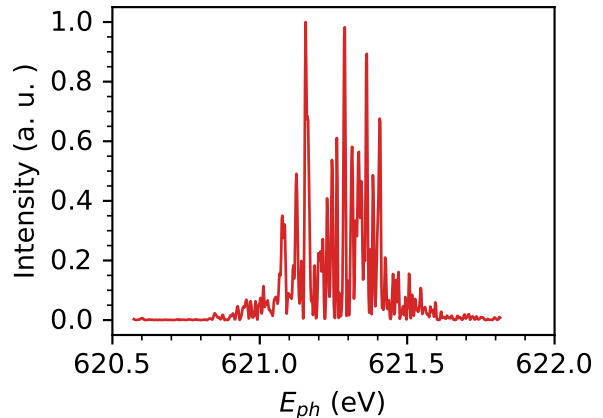


FIG. 3. Energy spectrum of FEL pulse.

photons, with an average energy and bandwidth around 621 and 0.8 eV, respectively.

To simulate the yield and the angular distribution of the photoionized electrons, we developed a Monte Carlo model within the framework of the Geant4 code and based on our previous research [19]. The geometry of the instrument was set up after reasonable simplifications. The ARPolar polarimeter contained 16 detection channels, where, for each channel, the incident hole was oriented toward the center of the beamline pipe and captured electrons traveling in a uniform angular direction. The vertices of the primary photons were located at the center of the chamber, and their energy was distributed as shown in Fig. 3. The ionization process instigated by the polarized photon was based on the G4Livermore polarized electromagnetic model combined with the cross-section dataset G4EMLOW-4.8 [31]. Table I summarizes the key parameters in the model. As long as the electrons enter

TABLE I. Main parameters of the Geant4-based Monte Carlo model.

Parameter	Value	Description
$D$	20 mm	Distance between the center of the beamline and the incident hole of a TOF channel.
$\phi_i$	3 mm	Diameter of the incident hole.
$\rho_{tg}$	$1.54 \times 10^{-11}$ kg/m <sup>3</sup>	Average gas density of the target.
$L_d$	400 mm	Drift length of photoelectrons.
$P_l$	1	Linear polarity.
$\theta_p$	0	Polarization angle.

ing the incident hole, the energies, directions, and positions of their primary vertex are recorded. The result indicates that 38% of photo-ionized electrons generated within the detection plane are captured in the detection channels because the flight distance before entering the detection hole is only 20 mm and the chamber is well shielded against stray magnetic fields. For the full linearly polarized FEL pulses, about  $10^4$  incident electrons enter the channel oriented along the polar-

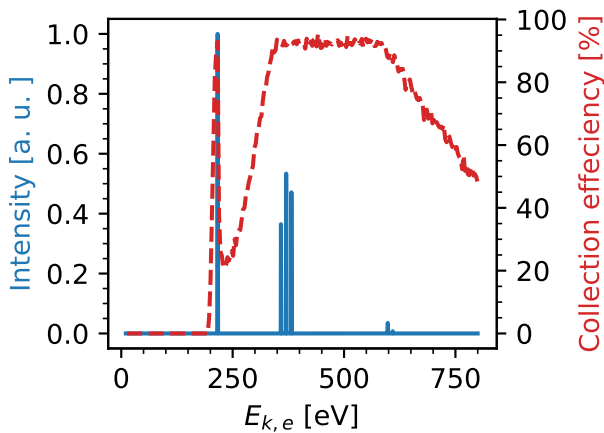


FIG. 4. Collection efficiency of electron-optical system.

ization direction, which suggests that the statistical fluctuation is sufficiently small to diagnose polarization and monitor position.

To simulate the collection efficiency of the electron-optical system, we developed a coupled static-electric, particle-tracing model using the SIMION software [32]. The model consists of three electrode groups A, B, and G and a drift tube. Electrodes of groups A and B are three ring-type electrodes that focus and filter electrons. Group G electrodes are two grid electrodes  $G_1$  and  $G_2$  that retard electrons for long time intervals that depend on the electron energy. The drift tube was 300 mm long and its voltage was floated with respect to ground and tuned to maintain the energy of the retarded electrons. The particle trajectories and the flight time were recorded to analyze the detection efficiency, which is defined as the ratio of the number of electrons collected by the MCP detectors to the number of electrons incident on the detection hole. For a  $N_2$  target and FEL pulses with an average energy of around 621 eV, the  $s$ -shell electron energy is about 217 eV, we designed an electron-optical system to optimize the collection efficiency for photo-electrons and Auger electrons. Figure 4 shows the tuned collection efficiency, which shows the electron-optical system covers both the photo-electrons window and the auger electrons window.

### B. Simulation results

We used the numerical model described above to simulate the position measurements, which we present below, followed by the results of the polarization correction. To validate the method described above, we now describe the result for the scanning incident positions.

Figures 5(a) and 5(b) show the spatial distributions of  $\eta_x$  and  $\eta_y$ . The ratio  $\eta_x$  increases linearly from  $-0.06$  to  $0.06$  as  $x$  goes from  $-1$  to  $1$  mm, and the correlation between  $\eta_x$  and  $y$  is sufficiently small to be ignored.  $\eta_y$  increases linearly from  $-0.08$  to  $0.08$  as  $y$  goes from  $-1$  to  $1$  mm, and the small corre-

lation between  $\eta_y$  and  $x$  can also be ignored. The linearity can also be reported in terms of the gentle variation of  $S_x$  (or  $S_y$ ). The sensitivity of  $\eta$  remains constant as  $x$  (or  $y$ ) varies within the region  $y \in [-1 \text{ mm}, 1 \text{ mm}]$  (or  $x \in [-1 \text{ mm}, 1 \text{ mm}]$ ), as shown in Figs. 5(c) and 5(d). These results also show that  $S_x$  and  $S_y$  are about  $5.9$  [%/mm] and  $7.8$  [%/mm], respectively. Figures 5(e) and 5(f) allow us to conclude that the absolute values of  $\delta_x$  and  $\delta_y$  are less than  $3 \times 10^{-3}$  and  $4 \times 10^{-3}$  mm, respectively. These figures also show that  $\delta_x$  ( $\delta_y$ ) is almost independent of  $y$  ( $x$ ), indicating that there is no need for a complicated position-dependent calibration. The values of  $S_x$  ( $S_y$ ) and  $\delta_x$  ( $\delta_y$ ) are the average value along the  $y$  ( $x$ ) axis. The unit vectors  $\hat{x}$  and  $\hat{y}$  were then calculated to predict position as per Eqs. (12) and (13), with the  $S_x = 5.9$  [%/mm],  $S_y = 7.8$  [%/mm],  $\delta_x = 0.003$  [mm],  $\delta_y = 0.004$  [mm], and  $\psi = 180^\circ$ . Figure 6 shows the absolute deviation of the predicted position  $(x, y)$ , in which  $x, y \in [-1 \text{ mm}, 1 \text{ mm}]$  are selected. The circles indicate the real  $x$ -ray position and the dots are calculated using Eq. (14).

The intensity and  $\gamma$  angle of each detector depends strongly on the polarity and the incident position. By correcting the incident position using Eqs. (15) and (16), the angular distribution  $p_s(\gamma)$  of photoelectrons is corrected and the FEL's polarization measurement improves. Figure 7 shows the original and corrected photoelectron angular distributions at the incident point  $(x, y) = (1, 1)$  mm. Fitting with Eq. (15) reveals a 40% enhancement of the linear polarity (from 0.979 to 0.985). Figure 8 shows the linear polarity of XFEL pulses along the axes oriented at  $45^\circ$  and  $135^\circ$ . These results show that the compensated value of  $P_l$  at all positions is close to  $P_l$  at  $(x, y) = (0, 0)$  mm, which indicates that the transverse position-compensation method may be used for pulse-to-pulse polarization diagnosis.

## IV. CALIBRATION METHOD

Conventional XFELs are fully horizontally and linearly polarized. Thus, the value of  $S_x$  and  $S_y$  can be precisely calibrated by using an external XBPM such as fluorescent screens or backscattering detectors. But it is challenging and time consuming to calibrate  $S_x$  (or  $S_y$ ) for polarization-modulated FEL pulses, which can be generated using an additional elliptically polarized undulator [33]. When the linear polarity  $P_l$  of an x-ray pulse varies, the variations in  $S_x$  and  $S_y$  are caused by the variations in the dipole-symmetric angular distribution of the photoelectrons. For a  $N_2$  target, Fig. 9 shows the relationship between  $S_x$  or  $S_y$  and the linear polarity, which suggests that  $S_x$  and  $S_y$  are linearly related to  $P_l$ . In particular,  $S_x = S_y = S_0$  when the FEL pulses are fully circularly polarized because the angular distribution of photoinduced electrons is isotropic. As for the  $N_2$  target, the photoionization cross section of the  $p$  shell is significantly smaller than that of the  $s$  shell [34, 35]. It is reasonable to describe the linear relationship between the  $S$  parameters and the linear polarity

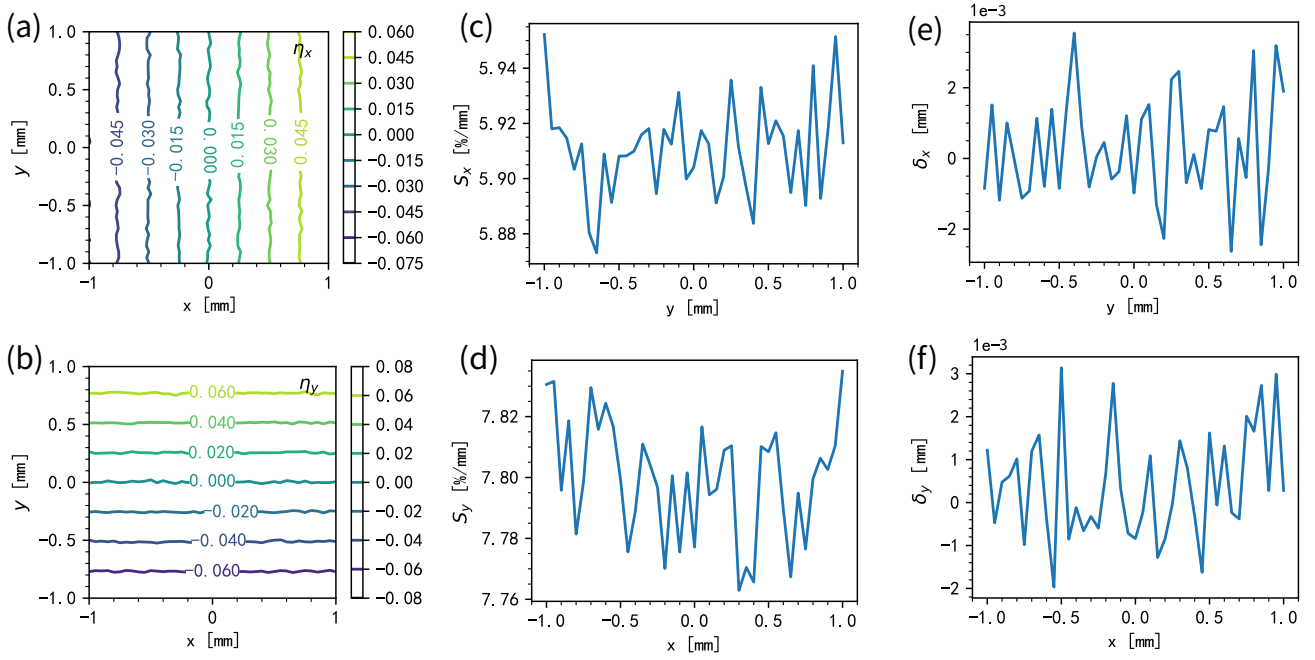


FIG. 5. Results of simulation of transverse position measurement. (a) Spatial distribution of  $\eta_x$ . (b) Spatial distribution of  $\eta_y$ . (c)  $S_x$  as a function of incident position  $y$ . (d)  $S_y$  as a function of incident position  $x$ . (e)  $\delta_x$  as a function of  $y$ . (f)  $\delta_y$  as a function of  $x$ .

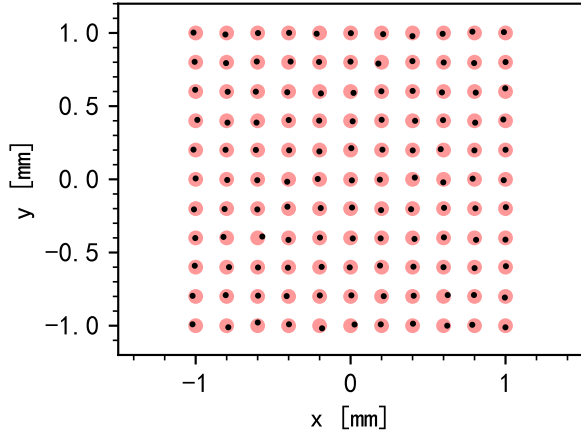


FIG. 6. Circles show the real x-ray positions and dots show the results of  $x = (1/S_x)\eta_x + \delta_x$ ,  $y = (1/S_y)\eta_y + \delta_y$  with the  $S_x = 5.9$  [%/mm],  $S_y = 7.8$  [%/mm],  $\delta_x = 0.003$  [mm],  $\delta_y = 0.004$  [mm].

$P_l$  as

$$S_x = S_0 + k_s P_l, \quad (18)$$

$$S_y = S_0 - k_s P_l, \quad (19)$$

where  $k_s = (S_{x,1} - S_0)/d_{P_l}$ , and

$$S_0 = \frac{1}{2}[S_x(P_l = 1) + S_y(P_l = 1)]. \quad (20)$$

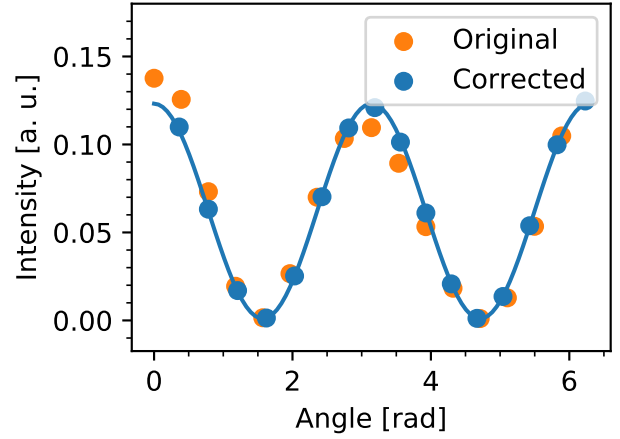


FIG. 7. Angular distribution of photoelectrons before and after compensation.

From the analysis above, the following approach can be applied to calibrate  $S_x$  and  $S_y$  for the  $N_2$  target: First, the sensitive values  $S_{x,1}$  and  $S_{y,1}$  for the fully linearly polarized FEL are calibrated and  $S_0$  is obtained by using Eq. (20). Next, the linear polarity without transverse position corrections  $P_{l,u}$  are measured and sensitivity values  $S_{x,1}$  and  $S_{y,1}$  are linearly interpolated using  $P_{l,u}$  and Eq. (18). Finally, the transverse position and the corrected polarization can be obtained by the compensation method described herein.

For the Ar target, the photoionization cross sections for the

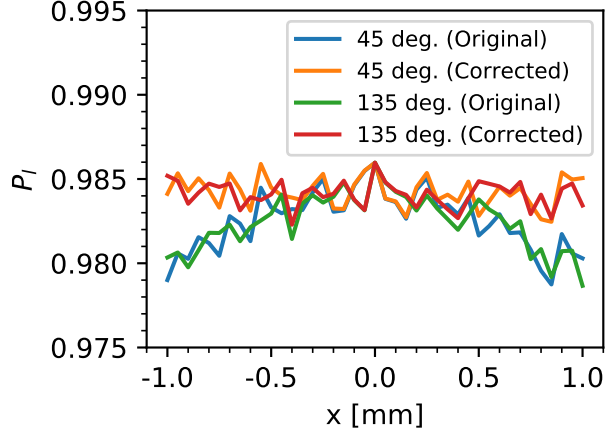


FIG. 8. Original and compensated linear polarity along  $45^\circ$  and  $135^\circ$  for horizontally polarized XFEL pulses.

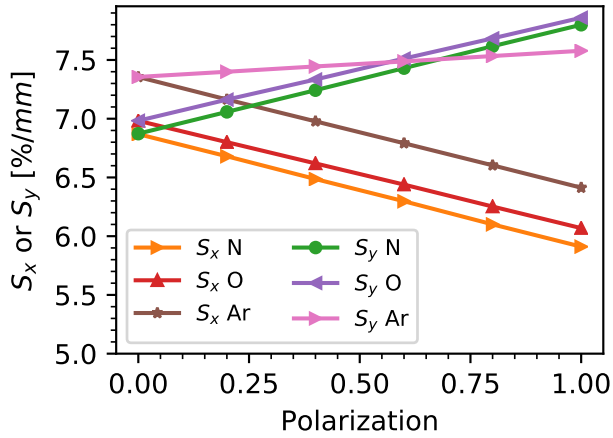


FIG. 9.  $S$  parameters of N, O, Ar as a function of linear polarization of FEL.

$p$  shells are of the same order of magnitude as those of the  $s$  shells, and Eqs. (18) and (20) are no longer applicable. Therefore, the sensitivities  $S_{x,0}$  and  $S_{y,0}$  should be calibrated additionally for a circular polarized FEL to obtain  $k_s$  despite electrons from the  $p$  shells being filtered by the electron-optical system.

## V. DISCUSSION AND CONCLUSION

Although the method presented in this work is fully feasible, there remain challenges and further improvements to be made, which we discuss below.

The linearity and the stability of the charge measurement strongly affect position monitoring and polarization diagnosis. The charge detected in a channel is given as

$$Q_i = n_e e \eta_{c,i} \eta_{p,i} G_i, \quad (21)$$

where  $n_e$  are the number of electrons captured in detection channel  $i$ ,  $e < 0$  is the fundamental charge of an electron,  $\eta_c$  is the collection efficiency of detection channel  $i$ ,  $\eta_p$  is due to the incident position, and  $G_i$  is the gain of the MCP detector of channel  $i$ . Because the electron-optical system can be configured with a precise static-electric bias, the collection efficiencies  $\eta_{c,i}$  are the same for all channels at the time of the measurement. Thus, the most significant factor for measuring charge is the gain  $G_i$  of the MCP detectors. As the capacity of residual charge decreases, the gain of the MCP detectors may decrease during the commissioning period. However, it is laborious to detach the polarimeter from the beamline and adjust the high-voltage power supplies to calibrate and ensure gain consistency for 16 channels using a well-known x-ray or electron source. A practical approach to calibrating the gain of the MCP detector is to use the MCP response to a single electron so that  $n_e = 1$  and  $\eta_{p,i} = 1$ . Single electrons can be obtained by adjusting the focusing electrodes.

Another factor that affects the position measurement is the yield of photoelectrons. As the number of photoelectrons increases, the statistical fluctuations increase, which suggests that a stronger FEL intensity and a high target density are preferable. In the current design of the ARPolar instrument, a specially designed skimmer serves to concentrate the gas direction, and two 700 L/s turbo pumps produce a target density of  $1.54 \times 10^{-11} \text{ kg/m}^3$ , as determined by a simulation with the well-benchmarked Molflow+ code [36]. Note that position monitoring for multiple pulses is acceptable for compensating polarization diagnosis because drift between the FEL machine states is sufficiently slow to measure the mass center of FEL pulses.

Methods exist to potentially measure position using an ARPolar-like instrument. Because electron energy can be reduced by using grid electrodes while their intensity is maintained by using focusing electrodes in the detection channels, a synchronized, fast-rise-time electric field in front of the MCP detector can be used to filter electrons with different flight times, such as is caused by the different flight distance between the transverse position of XFEL pulses and the detector.

This work thus describes methods and principles for single-shot transverse position measurements and compensation for diagnosing FEL polarization states. A comprehensive numerical model is presented to analyze the accuracy and stability of the method. Polarization compensation reduces the error in  $P_l$  by 40% compared with a direct diagnosis.

## ACKNOWLEDGMENTS

This work was funded by National Key Research and Development Program of China (Grant No. 2016YFA0401901), the National Natural Science Foundation of China (Grant No. 11775293), and the Ten Thousand Talents Program.

- [1] E. Allaria, B. Diviacco, C. Callegari, P. Finetti, B. Mahieu, J. Viehhaus, M. Zangrando, G. De Ninno, G. Lambert, E. Ferrari, J. Buck, M. Ilchen, B. Vodungbo, N. Mahne, C. Svetina, C. Spezzani, S. Di Mitri, G. Penco, M. Trovó, W. M. Fawley, P. R. Rebernik, D. Gauthier, C. Grazioli, M. Coreno, B. Ressele, A. Kivimäki, T. Mazza, L. Glaser, F. Scholz, J. Seltmann, P. Gessler, J. Grünert, A. De Fanis, M. Meyer, A. Knie, S. P. Moeller, L. Raimondi, F. Capotondi, E. Pedersoli, O. Plekan, M. B. Danailov, A. Demidovich, I. Nikolov, A. Abrami, J. Gautier, J. Lüning, P. Zeitoun, and L. Giannessi, *Physical Review X* **4**, 1 (2014).
- [2] H. Deng, T. Zhang, L. Feng, C. Feng, B. Liu, X. Wang, T. Lan, G. Wang, W. Zhang, X. Liu, J. Chen, M. Zhang, G. Lin, M. Zhang, D. Wang, and Z. Zhao, *Physical Review Special Topics - Accelerators and Beams* **17**, 1 (2014).
- [3] A. A. Lutman, J. P. MacArthur, M. Ilchen, A. O. Lindahl, J. Buck, R. N. Coffee, G. L. Dakovski, L. Dammann, Y. Ding, H. A. Dürr, L. Glaser, J. Grünert, G. Hartmann, N. Hartmann, D. Hügley, K. Hirsch, Y. I. Levashov, A. Marinelli, T. Maxwell, A. Mitra, S. Moeller, T. Osipov, F. Peters, M. Planas, I. Shevchuk, W. F. Schlotter, F. Scholz, J. Seltmann, J. Viehhaus, P. Walter, Z. R. Wolf, Z. Huang, and H. D. Nuhn, *Nature Photonics* **10**, 468 (2016).
- [4] N. Huang, K. Li, and H. Deng, *Physical Review Accelerators and Beams* **23**, 30702 (2020).
- [5] W. Ackermann, G. Asova, V. Ayvazyan, A. Azima, N. Baboi, J. Bähr, V. Balandin, B. Beutner, A. Brandt, A. Boltmann, R. Brinkmann, O. I. Brovko, M. Castellano, P. Castro, L. Catani, E. Chiadroni, S. Choroba, A. Cianchi, J. T. Costello, D. Cubaynes, J. Dardis, W. Decking, H. Delsim-Hashemi, A. Delsierieys, G. Di Pirro, M. Dohlus, S. Düsterer, A. Eckhardt, H. T. Edwards, B. Faatz, J. Feldhaus, K. Flöttmann, J. Frisch, L. Fröhlich, T. Garvey, U. Gensch, C. Gerth, M. Görler, N. Golubeva, H. J. Grabosch, M. Grecki, O. Grimm, K. Hacker, U. Hahn, J. H. Han, K. Honkavaara, T. Hott, M. Hüning, Y. Ivanisenko, E. Jaeschke, W. Jalmuzna, T. Jezynski, R. Kammering, V. Katalev, K. Kavanagh, E. T. Kennedy, S. Khodyachykh, K. Klose, V. Kocharyan, M. Körfer, M. Kollwe, W. Koprek, S. Korepanov, D. Kostin, M. Krassilnikov, G. Kube, M. Kuhlmann, C. L. Lewis, L. Lilje, T. Limberg, D. Lipka, F. Löhler, H. Luna, M. Luong, M. Martins, M. Meyer, P. Michelato, V. Miltchev, W. D. Möller, L. Monaco, W. F. Müller, O. Napieralski, O. Napoly, P. Nicolosi, D. Nölle, T. Nuez, A. Oppelt, C. Pagani, R. Paparella, N. Pchalek, J. Pedregosa-Gutierrez, B. Petersen, B. Petrosyan, G. Petrosyan, L. Petrosyan, J. Pflüger, E. Plönjes, L. Poletto, K. Pozniak, E. Prat, D. Proch, P. Pucyk, P. Radcliffe, H. Redlin, K. Rehlich, M. Richter, M. Roehrs, J. Roensch, R. Romaniuk, M. Ross, J. Rossbach, V. Rybnikov, M. Sachwitz, E. L. Saldin, W. Sandner, H. Schlarb, B. Schmidt, M. Schmitz, P. Schmüser, J. R. Schneider, E. A. Schneidmiller, S. Schnepf, S. Schreiber, M. Seidel, D. Sertore, A. V. Shabunov, C. Simon, S. Simrock, E. Sombrowski, A. A. Sorokin, P. Spänknebel, R. Spesyvtsev, L. Staykov, B. Steffen, F. Stephan, F. Stulle, H. Thom, K. Tiedtke, M. Tischer, S. Toleikis, R. Treusch, D. Trines, I. Tsakov, E. Vogel, T. Weiland, H. Weise, M. Wellhöfer, M. Wendt, I. Will, A. Winter, K. Wittenburg, W. Wurth, P. Yeates, M. V. Yurkov, I. Zagorodnov, and K. Zapfe, *Nature Photonics* **1**, 336 (2007).
- [6] P. Emma, R. Akre, J. Arthur, R. Bionta, C. Bostedt, J. Bozek, A. Brachmann, P. Bucksbaum, R. Coffee, F. J. Decker, Y. Ding, D. Dowell, S. Edstrom, A. Fisher, J. Frisch, S. Gilevich, J. Hastings, G. Hays, P. Hering, Z. Huang, R. Iverson, H. Loos, M. Messerschmidt, A. Miahnahri, S. Moeller, H. D. Nuhn, G. Pile, D. Ratner, J. Rzepiela, D. Schultz, T. Smith, P. Stefan, H. Tompkins, J. Turner, J. Welch, W. White, J. Wu, G. Yocky, and J. Galayda, *Nature Photonics* **4**, 641 (2010).
- [7] T. Ishikawa, H. Aoyagi, T. Asaka, Y. Asano, N. Azumi, T. Bizen, H. Ego, K. Fukami, T. Fukui, Y. Furukawa, S. Goto, H. Hanaki, T. Hara, T. Hasegawa, T. Hatsui, A. Higashiya, T. Hirono, N. Hosoda, M. Ishii, T. Inagaki, Y. Inubushi, T. Itoga, Y. Joti, M. Kago, T. Kameshima, H. Kimura, Y. Kirihara, A. Kiyomichi, T. Kobayashi, C. Kondo, T. Kudo, H. Maesaka, X. M. Maréchal, T. Masuda, S. Matsubara, T. Matsumoto, T. Matsushita, S. Matsui, M. Nagasono, N. Nariyama, H. Ohashi, T. Ohata, T. Ohshima, S. Ono, Y. Otake, C. Saji, T. Sakurai, T. Sato, K. Sawada, T. Seike, K. Shirasawa, T. Sugimoto, S. Suzuki, S. Takahashi, H. Takebe, K. Takeshita, K. Tamasaki, H. Tanaka, R. Tanaka, T. Tanaka, T. Togashi, K. Togawa, A. Tokuhisa, H. Tomizawa, K. Tono, S. Wu, M. Yabashi, M. Yamaga, A. Yamashita, K. Yanagida, C. Zhang, T. Shintake, H. Kitamura, and N. Kumagai, *Nature Photonics* **6**, 540 (2012).
- [8] C. Feng and H. X. Deng, *Nuclear Science and Techniques* **29** (2018), 10.1007/s41365-018-0490-1.
- [9] G. Schtz, W. Wagner, W. Wilhelm, P. Kienle, R. Zeller, R. Frahm, and G. Materlik, *Physical Review Letters* **58**, 737 (1987).
- [10] C. T. Chen, F. Sette, Y. Ma, and S. Modesti, *Physical Review B* **42**, 7262 (1990).
- [11] J. B. Kortright, D. D. Awschalom, J. Stöhr, S. D. Bader, Y. U. Idzerda, S. S. Parkin, I. K. Schuller, and H. C. Siegmann, *Journal of Magnetism and Magnetic Materials* **207**, 7 (1999).
- [12] B. S. Kang, D. H. Kim, E. Anderson, P. Fischer, and G. Cho, *Journal of Applied Physics* **98**, 2910 (2005).
- [13] A. Gaupp and M. Mast, *Review of Scientific Instruments* **60**, 2213 (1989).
- [14] T. Koide, T. Shidara, M. Yuri, N. Kandaka, K. Yamaguchi, and H. Fukutani, *Nuclear Inst. and Methods in Physics Research, A* **308**, 635 (1991).
- [15] H. Höchst and F. Middleton, *Nuclear Instruments & Methods in Physics Research* **347**, 107 (1994).
- [16] F. Schäfers, H.-C. Mertins, A. Gaupp, W. Gudat, M. Mertin, I. Packe, F. Schmolla, S. Di Fonzo, G. Soullié, W. Jark, R. Walker, X. Le Cann, R. Nyholm, and M. Eriksson, *Applied Optics* **38**, 4074 (1999).
- [17] B. Vodungbo, A. Barszczak Sardinha, J. Gautier, G. Lambert, C. Valentin, M. Lozano, G. Iaquaniello, F. Delmotte, S. Sebban, J. Lüning, and P. Zeitoun, *Optics Express* **19**, 4346 (2011).
- [18] J. Laksman, J. Buck, L. Glaser, M. Planas, F. Dietrich, J. Liu, T. Maltezopoulos, F. Scholz, J. Seltmann, G. Hartmann, M. Ilchen, W. Freund, N. Kujala, J. Viehhaus, and J. Grünert, *Journal of Synchrotron Radiation* **26**, 1010 (2019).
- [19] Q. Zhang, B. Deng, Y. Chen, B. Liu, S. Chen, J. Fan, L. Feng, H. Deng, B. Liu, and D. Wang, *Journal of Instrumentation* **12** (2017).
- [20] J. Laksman, J. Buck, L. Glaser, M. Planas, and J. Grünert, *Journal of Synchrotron Radiation* **26** (2019).
- [21] P. Walter, A. Kamalov, A. Gatton, T. Driver, D. Bhogadi, J. C. Castagna, X. Cheng, H. Shi, J. Cryan, and W. Helml, (2021).
- [22] N. Huang, H. Deng, B. Liu, D. Wang, and Z. Zhao, *The Innovation*, 100097 (2021).

- [23] R. W. Alkire, G. Rosenbaum, and G. Evans, *Journal of Synchrotron Radiation* **7**, 61 (2000).
- [24] P. Heimann, A. Reid, Y. Feng, and D. Fritz, *Journal of Synchrotron Radiation* **26**, 358 (2019).
- [25] Ilinski, P., Hahn, U., Schulte-Schrepping, H., Degenhardt, and M., *AIP Conference Proceedings* (2007).
- [26] K. Tono, M. Yabashi, T. Tachibana, Y. Feng, D. Fritz, J. Hastings, K. Tono, M. Yabashi, T. Tachibana, and Y. Feng, **023108** (2013), 10.1063/1.3549133.
- [27] R. E. Shafer, **26**, 601 (2008).
- [28] A. Gaupp, F. P. Wolf, and Bessy, *Synchrotron Radiation News* **1**, 27 (1988).
- [29] S. T. Manson and A. F. Starace, *Reviews of Modern Physics* **54**, 389 (1982).
- [30] J. W. Cooper, *Physical Review A* **47**, 1841 (1993).
- [31] D. Cullen, J. H. Hubbell, and L. Kissel, accessed (1997).
- [32] D. A. Dahl, J. E. Delmore, and A. D. Appelhans, *Review of Scientific Instruments* **61**, 607 (1990).
- [33] H. Deng, T. Zhang, L. Feng, C. Feng, B. Liu, X. Wang, T. Lan, G. Wang, W. Zhang, X. Liu, J. Chen, M. Zhang, G. Lin, M. Zhang, D. Wang, and Z. Zhao, *Physical Review Special Topics - Accelerators and Beams* **17**, 1 (2014).
- [34] I. M. Band, Y. I. Kharitonov, and M. B. Trzhaskovskaya, *Atomic Data and Nuclear Data Tables* **23**, 443 (1979).
- [35] M. B. Trzhaskovskaya, V. I. Nefedov, and V. G. Yarzhemsky, *Atomic Data and Nuclear Data Tables* **82**, 257 (2002).
- [36] R. Kersevan and J. L. Pons, *Journal of Vacuum Science & Technology A Vacuum Surfaces & Films* **27**, 1017 (2009).